TOMOGRAPHY® RESEARCH ARTICLE

# Experimental MRI Monitoring of Renal Blood Volume Fraction Variations *En Route* to Renal Magnetic Resonance Oximetry

**Andreas Pohlmann[1], Kathleen Cantow[2], Till Huelnhagen[1], Dirk Grosenick[3], João dos Santos Periquito[1], Laura Boehmert[1], Thomas Gladytz[3], Sonia Waiczies[1], Bert Flemming[2], Erdmann Seeliger[2], and Thoralf Niendorf[1,4,5]**

[1]Max Delbrück Center for Molecular Medicine in the Helmholtz Association, Berlin Ultrahigh Field Facility (B.U.F.F.), Berlin, Germany; [2]Institute of Physiology and Center for Cardiovascular Research, Charité – Universitätsmedizin Berlin, Campus Charité Mitte, Berlin, Germany; [3]Physikalisch-Technische-Bundesanstalt (PTB), Berlin, Germany; [4]Experimental and Clinical Research Center, Charité Medical Faculty and the Max Delbrück Center for Molecular Medicine in the Helmholtz Association, Berlin, Germany; and [5]Deutsches Zentrum für Herz- Kreislauf-Forschung (DZHK; German Centre for Cardiovascular Research), Berlin, Germany

**Corresponding Author:**
Andreas Pohlmann, PhD
Max Delbrück Center for Molecular Medicine in the Helmholtz Association, Robert Rössle Str. 10, 13125 Berlin, Germany;
E-mail: andreas.pohlmann@mdc-berlin.de

**Key Words:** kidney, oxygenation, blood volume fraction, magnetic resonance imaging, blood oxygenation level dependent (BOLD), ultrasmall superparamagnetic iron oxide (USPIO)

**Abbreviations:** Acute kidney injury (AKI), blood volume fraction (BVf), free induction decay (FID), magnetic resonance imaging (MRI), oxygen saturation of hemoglobin ($SO_2$), ultrasmall superparamagnetic iron oxide (USPIO), near-infrared spectroscopy (NIRS), signal-to-noise ratio (SNR), time-of-flight (TOF), venous occlusion (VO), radiofrequency (RF), repetition time (TR), echo time (TE), regions of interest (ROIs), multiecho gradient-echo (MGE), multi-spin echo (MSME)

ABSTRACT

Diagnosis of early-stage acute kidney injury (AKI) will benefit from a timely identification of local tissue hypoxia. Renal tissue hypoxia is an early feature in AKI pathophysiology, and renal oxygenation is increasingly being assessed through $T_2^*$-weighted magnetic resonance imaging (MRI). However, changes in renal blood volume fraction (BVf) confound renal $T_2^*$. The aim of this study was to assess the feasibility of intravascular contrast-enhanced MRI for monitoring renal BVf during physiological interventions that are concomitant with variations in BVf and to explore the possibility of correcting renal $T_2^*$ for BVf variations. A dose-dependent study of the contrast agent ferumoxytol was performed in rats. BVf was monitored throughout short-term occlusion of the renal vein, which is known to markedly change renal blood partial pressure of $O_2$ and BVf. BVf calculated from MRI measurements was used to estimate oxygen saturation of hemoglobin ($SO_2$). BVf and $SO_2$ were benchmarked against cortical data derived from near-infrared spectroscopy. As estimated from magnetic resonance parametric maps of $T_2$ and $T_2^*$, BVf was shown to increase, whereas $SO_2$ was shown to decline during venous occlusion (VO). This observation could be quantitatively reproduced in test–retest scenarios. Changes in BVf and $SO_2$ were in good agreement with data obtained from near-infrared spectroscopy. Our findings provide motivation to advance multiparametric MRI for studying AKIs, with the ultimate goal of translating MRI-based renal BVf mapping into clinical practice *en route* noninvasive renal magnetic resonance oximetry as a method of assessing AKI and progression to chronic damage.

## INTRODUCTION

Kidney diseases are a global health burden with steadily increasing incidence (1-4), leading to an estimated worldwide death toll of 2 million per year from AKI (5-7). The currently available methods of assessing risk and therapeutic options for AKI are limited (5, 6, 8-10). Although a number of biochemical markers are being evaluated for use in diagnosis, risk assessment, and prognosis of AKI, there are currently no specific biomarkers that permit point-of-care diagnosis for early-stage AKI (4, 11, 12). Translational approaches for the assessment of early-stage AKI and for the study of renoprotective strategies are urgently required (13-16). Strategies under consideration include novel imaging techniques that may be customized to probe early stages of AKI (12, 16-18).

Early features in the pathophysiology of AKI that could lend themselves to detection by noninvasive magnetic resonance (MR) imaging include renal tissue hypoperfusion and hypoxia—factors that are also important during the progression from AKI to chronic kidney diseases (16, 19-25). An imbalance between renal oxygen supply and demand appears to also play a prominent role in the pathophysiology of diabetic nephropathy (26). Renal oxygenation can be indirectly assessed through the blood oxygenation level-dependent (BOLD) magnetic resonance imaging (MRI) contrast (27), which can be observed through measurements of effective transversal relaxation time $T_2^*$. Indeed, mapping of renal $T_2^*$ (or its reciprocal, $R_2^* = 1/T_2^*$) is an established MRI method that is increasingly being used to study kidney disorders (28-30).


ISSN 2379-1381 http://dx.doi.org/10.18383/j.tom.2017.00012

Renal BOLD MRI is based upon the $T_2^*$ dependence on $O_2$ saturation of hemoglobin ($SO_2$) and motivated by the link between $SO_2$, blood partial pressure of $O_2$ ($pO_2$), and tissue $pO_2$. However, questions have been raised regarding the interpretation of BOLD MRI data in the kidney as a surrogate of tissue oxygenation (30). These concerns were triggered by the following recent findings from renal $T_2^*$ mapping: simultaneous renal $pO_2$ and $T_2^*$ measurements showed considerable discrepancies in the quantitative relationship between changes in renal $T_2^*$ and those in renal tissue $pO_2$ for different functional regions of the kidney and for various (patho)physiological scenarios (31). The renal $T_2^*$ to tissue $pO_2$ relationship is not governed exclusively by renal blood oxygenation, but it is also heavily influenced by a number of confounders (30, 31). Of particular importance are changes in the renal blood volume fraction (BVf). Renal $T_2^*$ reflects the amount of deoxygenated hemoglobin per tissue volume, and any variation in BVf compromises the interpretation of $T_2^*$ changes as reflecting alterations in blood oxygenation, or even tissue oxygenation. This essential role of renal BVf has been largely unheeded, although it was recently highlighted by reports on changes in renal vascular conductance, local hemoglobin concentrations, and kidney size induced by physiological interventions (31, 32). The impact of renal BVf changes on $T_2^*$ exceeds that of other organs' BVf owing to the considerably large BVf in the kidney (33). For these reasons, $T_2^*$ mapping alone cannot provide an unambiguous assessment of renal oxygenation.

A comprehensive renal MR oximetry protocol could have a quantitative value for the characterization of renal hemodynamics and tissue oxygenation if it integrates an assessment of renal BVf (30). Dynamic contrast-enhanced methods combined with tracer kinetic principles allow the quantification of renal perfusion and blood volume (34, 35) by using a bolus injection of exogenous agents like gadolinium chelates or iron oxide nanoparticles (36, 37). Analyzing the dynamic susceptibility contrast changes during bolus passage necessitates fast imaging with a temporal resolution of about 1 s, as well as measurement of the arterial concentration–time curve and its deconvolution from the tissue time curves. Renal dynamic susceptibility contrast was successfully implemented in dogs (36) and rats (37), but the methodological requirements limit the achievable spatial resolution and make this approach particularly challenging in small animals.

More recently, steady-state renal BVf measurements were performed by taking advantage of blood pool markers such as ultrasmall superparamagnetic iron oxide (USPIO) agents (38, 39); the change in transverse relaxation rate $R_2$ was examined in the kidney of mice (40) and rats (38). The steady-state approach comprises the simple subtraction of pre- and postcontrast maps of $R_2^*$ (41) (or $R_2$ if only small vessels are of interest), and it has the further benefit of facilitating the continuous monitoring of renal BVf (38). The USPIO nanoparticle preparation ferumoxytol has proven very useful for this (38, 42–45), as it can be administered intravenously without the risk of impaired renal oxygenation or perfusion (46), and it exhibits a long intravascular half-life of $>$14 h in humans and $\sim$2 h in small rodents (43, 44, 47).

The goal of the current study was to determine whether intravascular contrast-enhanced MRI can be used as a means of monitoring BVf in physiological settings, in which significant variations in both renal BVf and renal oxygenation are expected, and, furthermore, to explore the possibility of correcting renal BOLD measurements for BVf variations. A previous study by Storey et al. (38) used steady-state BVf monitoring during the administration of vasoactive drugs, but the induced $R_2$ variations (in the absence of USPIO) were attributed to changes in tubular volume fraction rather than BVf or oxygenation. Here, we investigate the feasibility of renal BVf monitoring in rat kidneys at 9.4 T as a means of achieving a comprehensive renal MR oximetry protocol. For this purpose, ferumoxytol-enhanced renal $T_2^*$ and $T_2$ mappings were performed under baseline conditions and after a short-term reversible intervention of renal vein occlusion. This intervention is known to cause marked changes in renal blood $pO_2$ and renal BVf. Local BVf was calculated on the basis of changes in $T_2^*$, which is equally sensitive to vessels of all sizes, unlike previous works that used $T_2$ (38, 40), which is more sensitive to small vessels (48). Local $SO_2$ of the kidney was estimated using a model-based multiparametric MR technique (49), and variations in BVf and $SO_2$ were benchmarked against reference data obtained from near-infrared spectroscopy (NIRS). Given the lack of information in the literature on a suitable ferumoxytol dose for renal BVf measurements at 9.4 T, we performed dosage experiments to establish a useful level of sensitivity to changes in BVf and $SO_2$.

## METHODOLOGY

### Animal Preparation and Control of Vital Functions

All experiments were approved by the Animal Welfare Department of the Berlin State Office of Health and Social Affairs and were performed in accordance with the German Animal Protection Law. The procuration of animals, husbandry, and experiments conformed to the *European Convention for the Protection of Vertebrate Animals used for Experimental and Other Scientific Purposes* (Council of Europe No 123, Strasbourg 1985). Male Wistar rats (age, 12–13 weeks; body weight [BW], 288–330 g; n = 4; Harlan-Winkelmann, Borchen, Germany) underwent surgical preparation and MRI under urethane anesthesia (20% in $H_2O$; 6 mL/kg BW intraperitoneal; Sigma-Aldrich, Steinheim, Germany). In this approach, anesthesia is provided for several hours, leaving cardiovascular reflexes largely undisturbed.

To monitor arterial blood pressure, a catheter was placed into the femoral artery with its tip pointing towards the aorta. The catheter was connected to a pressure transducer (DT-XX, Viggo-Spectramed, Swindon, UK) and an amplifier (TAM-A Plugsys Transducer; Hugo Sachs Elektronik—Harvard Apparatus GmbH, March-Hugstetten, Germany). A second catheter was inserted into the right jugular vein, which permitted the administration of isotonic saline and USPIO. Core body temperature was monitored within the abdominal cavity by means of a fiber-optic temperature probe (OTP-M, AccuSens, Opsens, Québec City, Canada). Body temperature was maintained at 37°C with a pad supplied with steady warm water circulation.

### Renal VO as Test Intervention

To induce renal VO during the MR study, a remotely operated inflatable cuff (occluder) was positioned around the left renal vein. Time-of-flight (TOF)-based MR angiography was performed immediately after cuff inflation and deflation to confirm the suc-

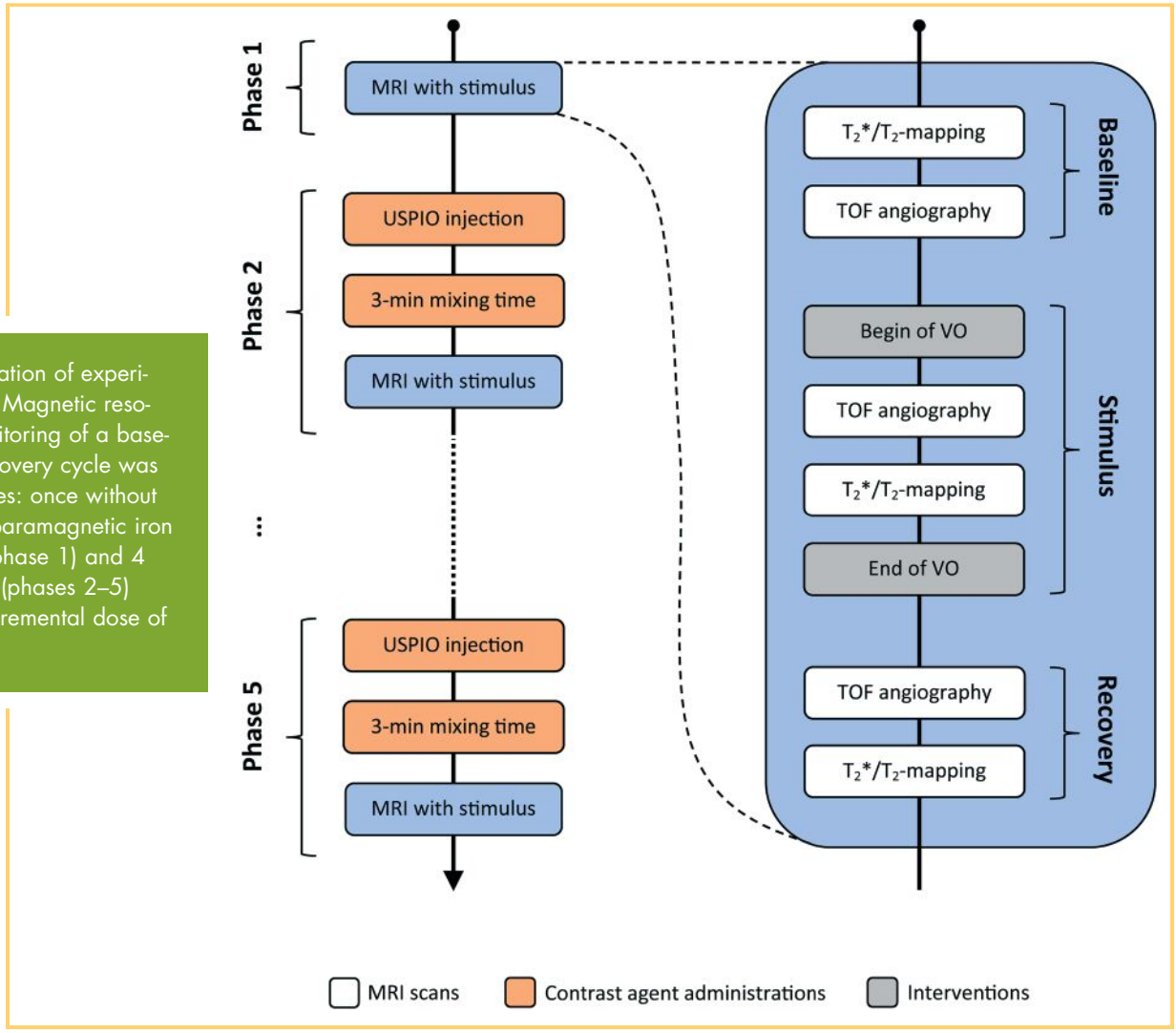


**Figure 1.** Illustration of experimental protocol. Magnetic resonance (MR) monitoring of a baseline–stimulus–recovery cycle was performed 5 times: once without ultrasmall superparamagnetic iron oxide (USPIO) (phase 1) and 4 successive times (phases 2–5) each with an incremental dose of USPIO.

cessful occlusion and reperfusion of the kidney. In the rare case of a failed occlusion, we could detect the problem quickly and could perform a second attempt of the stimulus without a substantial delay.

The occlusion of the renal vein is known to induce both deoxygenation of the intrarenal blood and a substantial increase in intrarenal blood volume (32). Cessation of the venous outflow of blood increases blood pressure in intrarenal veins, thus resulting in their circular distension. The increased amount of deoxygenated blood in the renal tissue amplifies the BOLD effect, which induces a reduction in the $T_2^*$-weighted MR signal in response to VO. A further reduction in the MR signal due to $T_2^*$ shortening induced by the USPIO might lower the signal-to-noise ratio (SNR) to a critical level at which the MR image/data quality might become insufficient. Therefore, VO in combination with USPIO represents an extreme scenario with respect to the expected $T_2^*$ shortening.

## BVf Measurement

BVf was measured using the USPIO ferumoxytol (Feraheme®, AMAG Pharmaceuticals, Inc., Lexington, MA). Ferumoxytol is approved in the USA and the EU as an intravascular Fe supplement therapy for patients with iron deficiency anemia related to chronic kidney disease. The intravenous injection of ferumoxytol does not have any measurable effects on renal physiology at doses up to 41 mg Fe/kg BW in rats; the presence of ferumoxytol also does not significantly alter the control of renal hemodynamics and oxygenation as studied by aortic occlusion and hypoxia (46).

Renal BVf was calculated by comparing pre-ferumoxytol data ($R_2^*$-maps) with post-ferumoxytol data ($R_{2USPIO}^*$-maps) (41):

$$BVf = \frac{3}{4\pi} \cdot \frac{(R^*_{2,USPIO} - R^*_2)}{\Delta\chi_{USPIO} \cdot B_0 \cdot \gamma} = \frac{3}{4\pi} \cdot \frac{\Delta R^*_{2,USPIO}}{\Delta\chi_{USPIO} \cdot B_0 \cdot \gamma} \quad (1)$$

where $\gamma$ is the gyromagnetic ratio, which is $2.675 \times 10^8$ rad/(s T); $B_0 = 9.4$ T; and $\Delta\chi_{USPIO}$ is the susceptibility difference between blood with and without added USPIO: $\Delta\chi_{USPIO} = 0.024$ ppm (cgs units) × [USPIO dose in milligram Fe per kilogram BW] (50).

## Ferumoxytol Dose-Finding Study

Considering the lack of information on a suitable ferumoxytol dose for renal BVf measurements at 9.4 T, we performed a dose-finding study. To accomplish this, the following 3 competing effects had to be balanced:

(1) sensitivity of the BVf measurements increases with the USPIO dose;
(2) the SNR of MR images decreases with the USPIO dose; and
(3) sensitivity to changes in BVf also decreases at high USPIO doses because $T_2^*$ tends to zero.

For these reasons, a ferumoxytol dose ranging from 2 to 8 mg Fe/kg BW was used.

## Experimental Protocol

The experimental protocol comprised 5 phases with increasing cumulative doses of ferumoxytol as illustrated in Figure 1:

(1) *Phase 1*: Baseline–stimulus–recovery without USPIO

(a) Baseline $T_2^*$ and $T_2$ mapping and TOF MR angiographic confirmation of renal blood flow.
(b) VO performed by remote inflation of the cuff.
(c) The absence of renal blood flow was checked immediately using TOF MR angiography.
(d) $T_2^*$ and $T_2$ mapping during VO.
(e) Release of the venous cuff. Effective duration of VO was ~3 min (depended on acquisition time of respiration-gated MRI scans performed in steps c and d).
(f) Restoration of renal blood flow was checked by TOF angiography
(g) Recovery phase, during which $T_2^*$ and $T_2$ mapping was continued: 5 repetitions, approximately every 3 mins covering a 12- to 14-min period (dependent of respiratory rate because scans were respiration-triggered)

(2) *Phase 2*: Baseline–stimulus–recovery with first USPIO dose

(h) The intravascular contrast agent (USPIO; 2 mg of Fe/kg body mass) was administered using a power injector at a rate of 0.25 mL/min via the jugular vein catheter.
(i–o) Following the conclusion of the injection and an additional 3-min mixing time, the steps of phase 1 were repeated to obtain matching post-USPIO data for phase 1.

(3) *Phase 3*: Baseline–stimulus–recovery with second USPIO dose

Same as phase 2 but with a different USPIO dose: the additional injection of 2 mg of Fe/kg USPIO yielded the approximate cumulative dose of 4 mg of Fe/kg USPIO (owing to the long half-live of the USPIO).

(4) *Phase 4*: Baseline–stimulus–recovery with third USPIO dose

Same as phase 2 but with a different USPIO dose; the additional injection of 2 mg of Fe/kg USPIO yielded an approximate cumulative dose of 6 mg of Fe/kg USPIO.

(5) *Phase 5*: Baseline–stimulus–recovery with fourth USPIO dose

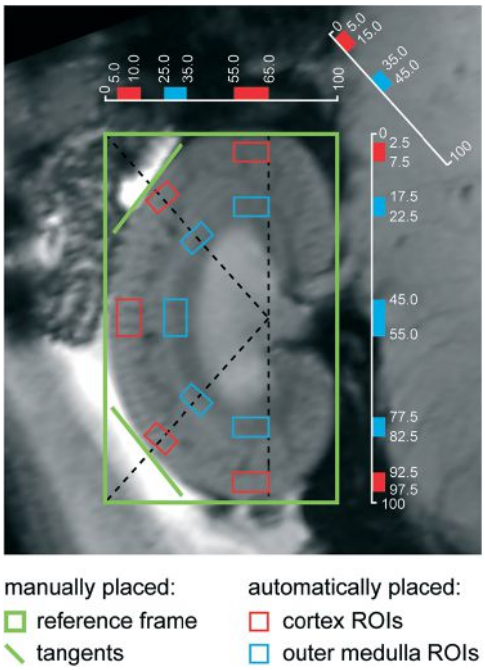


**Figure 2.** Semiautomated kidney segmentation. A region-of-interest (ROI) analysis was performed to obtain representative mean values for each renal layer. Guided by a manually drawn reference frame and tangents, 10 ROIs were placed automatically at locations in the cortex and outer medulla. The ROI locations were chosen on the basis of measurements taken on excised kidneys and histological sections of Wistar rat kidneys. ROI positions are given in percentages of the reference frame and diagonals.

Same as phase 2 but with a different USPIO dose; the additional injection of 2 mg of Fe/kg USPIO yielded the approximate cumulative dose of 8 mg of Fe/kg USPIO.

The duration of the experimental phase was ~20 min, which is short in comparison to the duration of the plasma half-life of ferumoxytol in rats (up to 3 h) (38).

## MR Imaging Experiments

MRI experiments were performed on a 9.4 T animal MR system (Biospec 94/20, Bruker Biospin, Ettlingen, Germany) using a radiofrequency (RF) coil setup established for renal imaging (linear polarized birdcage RF resonator for transmission in conjunction with a curved 4-channel receive RF coil array; Bruker Biospin, Ettlingen, Germany).

$T_2$-weighted pilot scans for geometrical planning and section positioning were acquired. We conducted a local volume-selective shimming of the magnetic field homogeneity on a voxel enclosing only the kidney, using an automatic optimization algorithm based on the FID length.

Interleaved $T_2^*$ and $T_2$ mapping was performed with respiratory-gated (Model 1025, SA Instruments, Stony Brook, NY) imaging protocols. For $T_2^*$ mapping, a multiecho gradient-echo

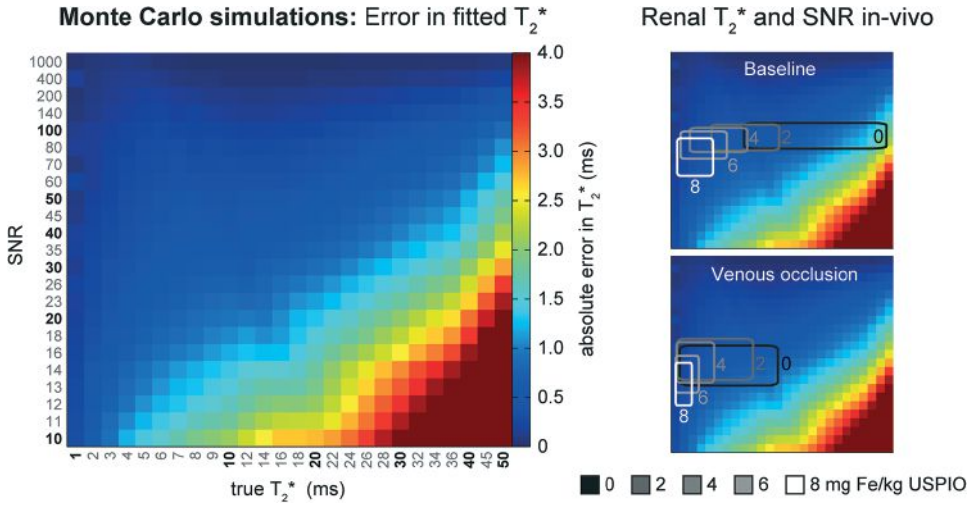


**Figure 3.** Left: Monte Carlo simulations were used to estimate the error in the fitted $T_2^*$ versus the true $T_2^*$ for a wide range of signal-to-noise ratios (SNRs). Each color-coded "pixel" in the matrix represents a simulated combination of true $T_2^*$ (1–50 milliseconds) and SNR (10 to 1000). The color indicates the mean absolute error in 10 000 $T_2^*$ fit simulations. Right: Overlaid boxes outline the typical ranges of $T_2^*$ and SNR measured in vivo at different Fe doses. In vivo, the cortical and outer medullary $T_2^*$ error is <1 millisecond.

(MGE) sequence (repetition time [TR] = 50 milliseconds; number of echoes = 10; first echo time [TE] = 1.43 milliseconds; ΔTE = 2.14 milliseconds; averages = 4) with a total acquisition time of ~1 min 20 s was used. For $T_2$ mapping, a multi-spin echo (MSME) sequence (TR = 550 milliseconds; number of echoes = 7; first TE = 10 milliseconds; ΔTE = 10 milliseconds; averages = 1) with a total acquisition time of around 1 min 40 s was applied. For MGE measurements, the respiratory trigger window included the entire expiratory plateau, which allowed for the acquisition of several k-space lines within this window. For MSME measurements, the respiratory trigger window was set to 10 milliseconds at the beginning of the expiratory plateau, resulting in the acquisition of 1 k-space line per breath, with the effective TR being equal to the respiratory interval.

A coronal oblique section was placed such that it covered the kidney centrally at its maximum extension. An in-plane spatial resolution of (226 × 445) $\mu m^2$, field of view = (38.2 × 50.3) $mm^2$, matrix size = 169 × 113 zero-filled to 169 × 215, and a section thickness of 1.4–1.5 mm was used.

For TOF angiography, we used a spoiled gradient echo technique (2D FLASH; TR = 11 milliseconds; TE = 3 milliseconds; flip angle = 80°) with a spatial in-plane resolution of (200 × 268) $\mu m^2$ and 15 sections (section thickness = 1.0 mm).

## Region of Interest Analysis

We extended the semiautomated kidney segmentation approach used in our previous studies (31, 51) to provide 5 regions of interest (ROIs) in the renal cortex and 5 ROIs in the renal outer medulla (Figure 2). In brief, a rectangle was manually placed around the kidney borders, followed by drawing lines at the crossing of the kidney border and 2 automatically placed diagonals. Further, 10 ROIs were placed automatically at locations in the cortex and outer medulla that had been predefined with respect to the reference rectangle.

## Effects of Magnetic Field Inhomogeneity on Renal $T_2^*$

Three-dimensional mapping of $B_0$ was performed to correct the $B_0$ inhomogeneity effects on $T_2^*$ (49). This $B_0$ correction involves (i) acquiring a 3D $B_0$ map of the kidney; (ii) estimating intra-voxel field dispersion across the kidney by fitting a 3D polynomial to the $B_0$ map; (iii) calculating intravoxel dephasing; and (iv) using this for correcting the measured $T_2^*$ map of the kidney.

To assess the need for $B_0$ correction in renal $T_2^*$ mapping, we performed $B_0$ correction on a kidney for different shim settings and compared the corrected renal $T_2^*$-maps with the measured, uncorrected $T_2^*$-maps. All shims were first set to zero to allow for significant $B_0$ inhomogeneities, and then first-order local shimming was performed on a voxel tightly enclosing the kidney to make $B_0$ uniform across the kidney. The latter was performed 3 times to account for any variability. A 3D polynomial function of the third order was fitted to the measured 3D $B_0$ map (in-house developed program; MATLAB, MathWorks, Natick, WA). This polynomial function was used to estimate the spin dephasing on a subvoxel grid of 2 × 2 × 4 voxels per image voxel (voxel size = 0.22 × 0.23 × 1.40 $mm^3$). Subvoxel grids finer than 2 × 2 × 4 did not yield significantly different results.

## Model-Based MRI Data Analysis

Multiecho MR data were converted into parametric maps of absolute $T_2^*$ and $T_2$ by pixelwise monoexponential fitting to the signal intensities of denoised (SANLM filter, VBM8 toolbox, SPM8; www.fil.ion.ucl.ac.uk/spm) series of $T_2^*$- and $T_2$-weighted images acquired as a function of the TE (in-house developed program; MATLAB, MathWorks, Natick, WA). The relaxation rates were calculated as $R_2^* = 1/T_2^*$ and $R_2 = 1/T_2$. The subtraction of precontrast maps from corresponding postcontrast maps yielded $\Delta R_2^*$-maps, which were used for the calculation of BVf-maps using equation (1).

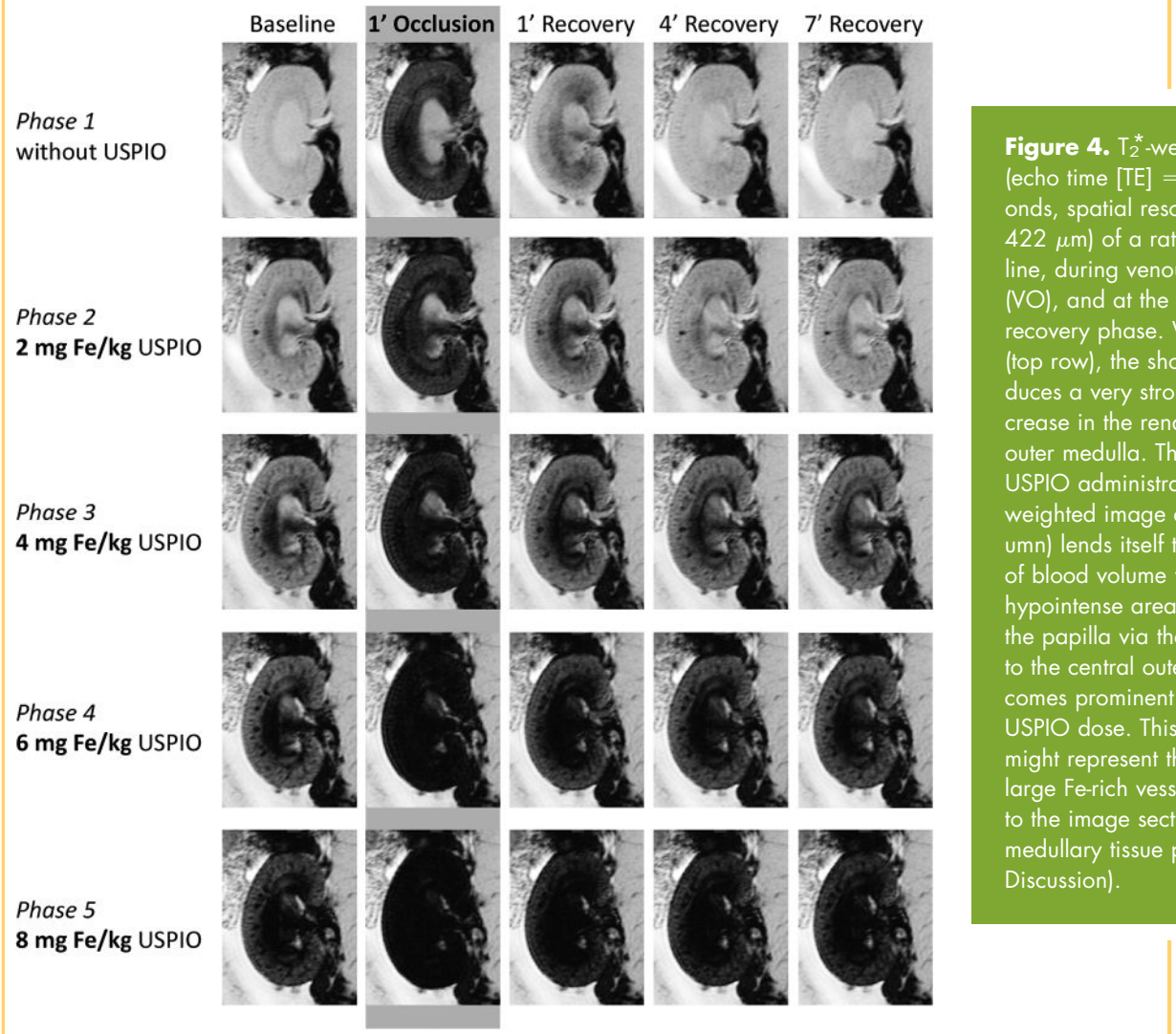


**Figure 4.** $T_2^*$-weighted images (echo time [TE] = 3.6 milliseconds, spatial resolution = 226 × 422 $\mu$m) of a rat kidney at baseline, during venous occlusion (VO), and at the beginning of the recovery phase. Without USPIO (top row), the short-term VO induces a very strong signal decrease in the renal cortex and the outer medulla. The impact of USPIO administration on $T_2^*$-weighted image contrast (left column) lends itself to an estimation of blood volume fraction (BVf). A hypointense area stretching from the papilla via the inner medulla to the central outer medulla becomes prominent with increasing USPIO dose. This hypointensity might represent the influence of large Fe-rich vessels located close to the image section rather than medullary tissue properties (see Discussion).

Renal blood $SO_2$ was estimated by applying a multiparametric MR technique (49) to the $R_2^*$, $R_2$ and BVf data from the kidney. This approach was originally proposed for human brain MRI (52) and is based on a theoretical model of the BOLD contrast (53). This approach was refined by replacing a complex model fit with a simpler single parameter fit combined with actual MR measurements of $R_2$, BVf, and $B_0$ (49). Assuming that the magnetic field inhomogeneity is negligible and constant throughout the duration of the experiment, we solved the model equation $s(t) = f(t, BVf, SO_2, \ldots)$ for $SO_2 = f(R_2^*, R_2, BVf, \ldots)$:

$$SO_2 \approx 1 - \left( \frac{3}{4\pi} \cdot \frac{(R_2^* - R_2)}{\gamma \cdot \Delta\chi_0 \cdot BVf \cdot Hct \cdot B_0} \right) \qquad (2)$$

Here $\Delta\chi_0 = 0.264$ ppm (54), which represents the susceptibility difference between deoxygenated and oxygenated red blood cells, $B_0 = 9.4$ T, and $SO_2$ is given in arbitrary units (because $B_0$ is uncorrected). A hematocrit of 0.40 was used for the cortex and the outer medulla (85%–95% of systemic hematocrit, which was assumed to be 0.45) (55). In this feasibility study, the data analysis was performed using equations (1) and (2), as these permit access to both parameters of interest, that is, $SO_2$ and BVf.

To evaluate intrasubject reproducibility, we compared results from the baseline with those obtained after 10 min of recovery and also repeated the baseline–occlusion–recovery experiment (~25 min later). Moreover, before repeating the experiment, we increased the USPIO dose by 2 mg Fe/kg BW to assess the dependency of the results on the USPIO dose.

## NIRS

Quantitative information on the relative changes of total cortical hemoglobin per tissue volume (as a surrogate for BVf) and cortical $SO_2$ during VO were obtained using multidistance continuous wave NIRS in a separate cohort of 10 male Wistar rats. The NIRS measurements are based on recording spatially resolved diffuse reflectance with a linear fiber probe. This probe permitted sampling of the renal tissue up to a maximum depth of ~2 mm and provided information about the renal cortex. The results presented here were obtained by a refined model analysis of data reported in Grosenick et al. (32), with improved separation of tissue absorption changes from changes in tissue scattering. To reference our results against these data, the high-temporal-resolution NIRS data were averaged over the duration of each MGE MRI scan.

## RESULTS

### Ferumoxytol Dose-Finding Study

The dose-finding study was performed to ensure that BOLD effects were detectable after USPIO administration taking into account that SNR may be further reduced by changes in $T_2^*$ owing to the deoxygenation of blood. By performing Monte Carlo simulations for a wide range of $T_2^*$ and SNR, we estimated the SNR-dependence of the $T_2^*$ mapping error (Figure 3).

$$\Delta T^*_{2,\text{error}} = T^*_{2,\text{calc}} - T^*_{2,\text{true}} \quad (3)$$

with "true" indicating the true $T_2^*$ value used as an input and "calc" indicating the $T_2^*$ value calculated by curve fitting to the noisy signal intensity data versus TE. For cortical and outer medullary $T_2^*$ the absolute error in $T_2^*$ was <1.0 milliseconds.

### $T_2^*$-Weighted MR Imaging

We observed a significant change in contrast and image quality following short-term VO and after increasing USPIO concentrations (Figure 4). VO caused a very strong signal decrease in the renal cortex and in the outer medulla. Even after a USPIO administration of 4 or 6 mg of Fe/kg BW, the strength of this decrease of the signal during VO remained similar and was easily detectable. Although the signal loss suggested renal hypoxia, that is, a decrease in oxygen saturation of hemoglobin, this remained speculative because, at this point, possible changes in BVf had not been considered. Comparing the $T_2^*$-weighted images at baselines for different USPIO doses shows the impact of USPIO administration on image contrast, which lends itself to an estimation of BVf.

Important for estimating the BVf is the sensitivity for detecting the change in $T_2^*$ caused by labeling the blood with USPIO. As expected, a larger USPIO dose provided more sensitivity for the measurement of:

$$\Delta T^*_{2,\text{USPIO}} = T^*_{2,\text{USPIO}} - T^*_2 \quad (4)$$

because the larger the cumulative USPIO dose, the larger the change in $T_2^*$ compared with the baseline (Figure 5A). This $T_2^*$ change was more pronounced in the outer medulla than in the renal cortex. In contrast to the sensitivity to USPIO effects, the sensitivity to changes in $T_2^*$ induced by VO decreased rapidly with the Fe dose (Figure 5B):

$$\Delta T^*_{2,\text{VO}} = T^*_{2,\text{VO}} - T^*_{2,\text{baseline}} \quad (5)$$

The sensitivity to changes in $T_2^*$ induced by VO fell below $\Delta T_2^* = 2.0$ milliseconds in the outer medulla for USPIO doses of 6 mg of Fe/kg and more. The relative $\Delta T_2^*$, as percentage of baseline $T_2^*$, did not change much and stayed between ~60% and 80%.

Considering the sensitivity of $T_2^*$ to USPIO injection (relevant for BVf estimation) and the $T_2^*$ sensitivity to the physiological stimulus, that is, VO, a USPIO dose of 4 mg of Fe/kg BW was chosen for estimating $R_2^*$ and ultimately for the BVf- and $SO_2$-maps.

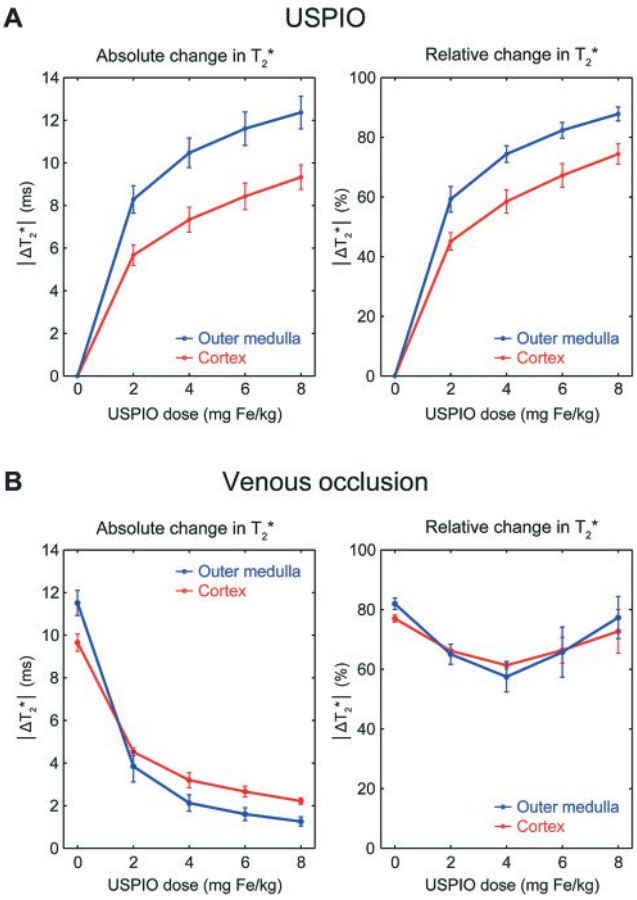


**Figure 5.** Comparison of the $T_2^*$ sensitivity to USPIO injection (relevant for BVf estimation) and the $T_2^*$ sensitivity to VO (physiological stimulus) at different cumulative USPIO doses. Plots of changes in cortical and outer medullary $T_2^*$ induced by the injections of USPIO (A). Absolute $\Delta T_2^*$ in milliseconds (left panel) and relative $\Delta T_2^*$ as percentage of $T_2^*$ without USPIO (right panel) increased rapidly with USPIO dose. Plots of changes in cortical and outer medullary $T_2^*$ induced by VO ($T_2^*$ values during a given VO versus $T_2^*$ before the respective VO) (A). Although absolute $\Delta T_2^*$ in milliseconds (left panel) decreased with USPIO dose, the percentage $\Delta T_2^*$ (right panel) remained between ~60% and 80%. Group means and SEMs (n = 4) of cortical and outer medullary $\Delta T_2^*$ obtained from the ROIs are determined as shown in Figure 2.

### Effects of Magnetic Field Inhomogeneity on Renal $T_2^*$

Macroscopic gradients in the magnetic field $B_0$—for instance, owing to imperfect $B_0$ shimming—may cause undesirable spin dephasing and could artificially shorten $T_2^*$. Before mapping renal $R_2^*$, BVf, and $SO_2$, we tested whether the susceptibility weighting and $T_2^*$ were dominated by microscopic $B_0$ susceptibility gradients. We investigated whether $B_0$ correction could reverse unwanted magnetic field inhomogeneity effects on $T_2^*$ by comparing measured and corrected renal $T_2^*$-maps acquired in vivo for different magnetic field shim settings as shown in Figure 6.

The 3D polynomial fits to the measured $B_0$-maps described the magnetic field inhomogeneity with high fidelity. A notable

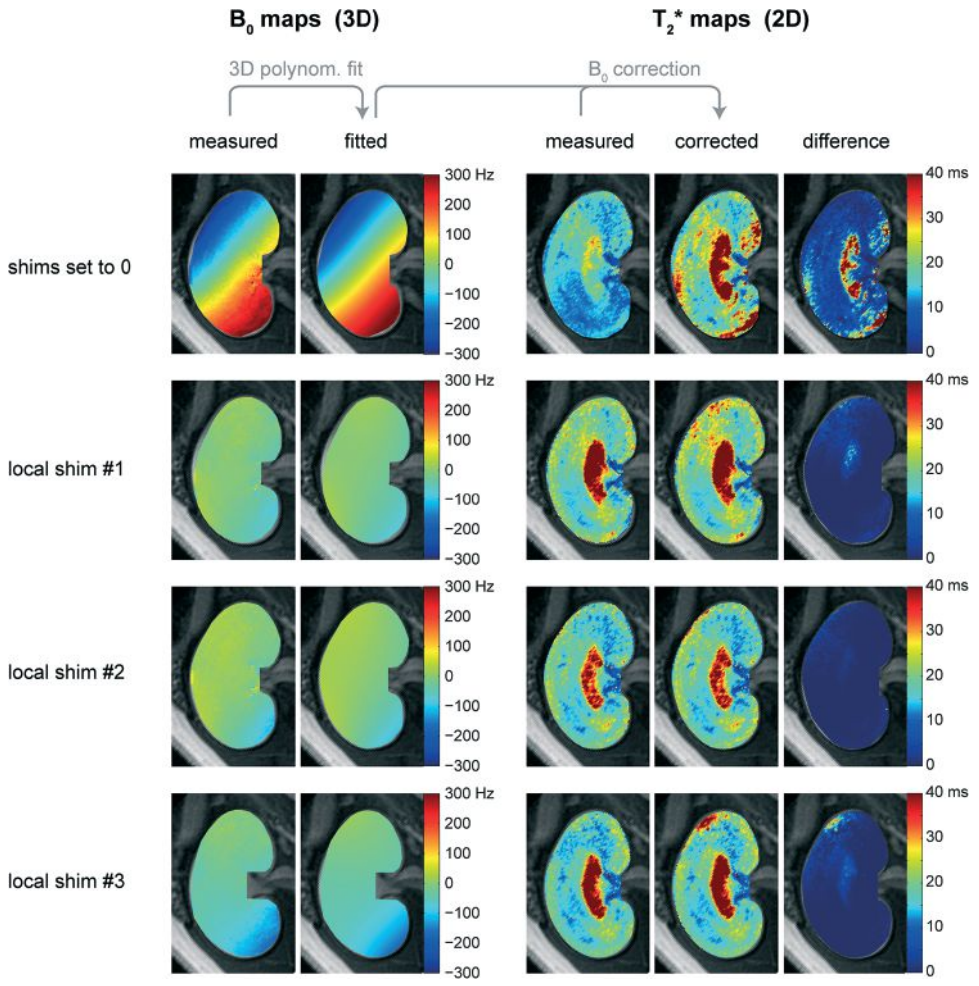


**Figure 6.** $B_0$ correction for removing macroscopic magnetic field inhomogeneity effects on $T_2^*$. Fitting a 3D polynomial function to the measured $B_0$ map permits calculation of the intravoxel magnetic field distribution. The spin dephasing caused by unwanted macroscopic gradients can then be calculated and used to correct the measured $T_2^*$. The parameter maps illustrate the $B_0$ correction performed for $T_2^*$ mapping of a rat kidney in vivo. Four different shim settings were used: all shims set to 0 (top row) and a first-order local shim on a voxel tightly enclosing the kidney, which was performed 3 times (rows 2–4) to assess variability. In the absence of shimming, the difference between the measured and corrected $T_2^*$-maps was notable. In contrast, the difference between measured and corrected $T_2^*$-maps was only minor when local shimming on the kidney had been performed.

macroscopic magnetic field inhomogeneity was present with the shim settings adjusted to zero. For this shim setting, $B_0$ correction markedly increased $T_2^*$, particularly in the inner medulla, where $T_2^*$ is typically large. $B_0$ inhomogeneity across the kidney was very small after local shimming on the kidney. After $B_0$ correction, the renal $T_2^*$-maps obtained for all 3 $B_0$ shim settings displayed high agreement. For local shimming, which we perform routinely in renal MR studies, the effect of $B_0$ correction on $T_2^*$ was negligible. This confirms that macroscopic intravoxel dephasing causes only minor $T_2^*$ effects for the TE range and the voxel size used and ensures that $T_2^*$ is governed by microscopic $B_0$ susceptibility gradients.

### Renal $R_2^*$, $R_2$, BVf, and $SO_2$ Mapping

Parametric maps were calculated for renal $T_2$ and $T_2^*$, which were then converted to $R_2$- and $R_2^*$-maps, respectively. Such quantitative maps permit comparisons between animals and over time, as they are not biased by external factors such as RF coil sensitivity ($B_1^-$) or the position of the subject under investigation with respect to the receive RF coil. The difference between $R_2^*$- and $R_2$-maps ($\Delta R_2^*$ and $\Delta R_2$, respectively), acquired before and after USPIO administration is closely related to the local BVf. The blood volume measurement procedure is illustrated in Figure 7, which shows parametric maps of renal $R_2$ and $R_2^*$ relaxation rates under baseline conditions, without and with USPIO (4 mg of Fe/kg), along with their difference. Dissimilarities between $\Delta R_2^*$ and $\Delta R_2$ are expected owing to their different sensitivities to large vessels (see Discussion).

Analysis of BVf-maps obtained at baseline and during renal VO (Figure 8) revealed an increase in cortical and medullary BVf upon VO. Renal BVf returned to baseline after 10 min of recovery. Next, maps of renal $SO_2$ were calculated using the multiparametric BOLD model outlined in equation (2), which requires $T_2^*$ and BVf as input data to analyze $SO_2$ at baseline, upon VO and on recovery (Figure 8). The reduction in renal $T_2^*$ during VO was associated with a decrease in $SO_2$ in the cortex and outer medulla combined with a substantial increase in blood volume.

To show the necessity of monitoring BVf (rather than using a fixed literature value), we also calculated $SO_2$-maps that assume renal BVf to remain constant and identical to the baseline condition during the entire experiment (Figure 8, lower panel). Almost everywhere in the cortex and outer medulla, $SO_2$ values were considerably lower in the experiments neglecting BVf changes compared with experiments taking BVf changes into account.

Reproducibility of results was very high: the results obtained for the cortical and outer medullary BVf and $SO_2$ at baseline conditions and after 10 min of recovery were almost

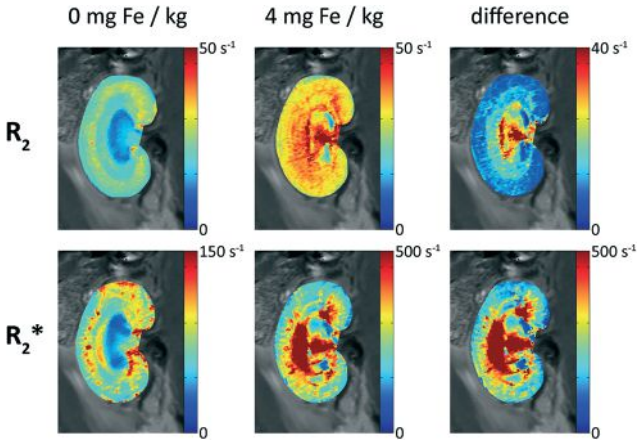


**Figure 7.** Illustration of blood volume measurement procedure. Shown are parametric maps of renal $R_2$ and $R_2^*$ at baseline. Quantitative maps permit comparisons over time and between animals, as they are not biased by external factors such as the RF coil sensitivity ($B_1^-$) or the location of the subject with respect to the RF coil. The difference between $R_2$-/$R_2^*$-maps acquired before and after USPIO is closely related to the local BVf. For a discussion of the apparent high-BVf area, stretching from the papilla via the inner medulla to the central outer medulla, please refer to the Discussion section.

indistinguishable (Figure 8). This finding is strengthened by the test–retest reliability (with 4 and 6 mg of Fe/kg BW USPIO): differences between both iterations were practically negligible, despite the fact that USPIO had been injected in between them. This result confirmed that the BVf calculation appropriately accounted for the effect of the USPIO dose. In the parameter maps, the inner medulla is not shown, as no justifiable assumptions about the hematocrit and liquid fraction in this region could be made. In our study, as well as in previous reports, the inner medullary $R_2$ was much higher than cortex and outer medulla $R_2$, suggesting high water content. This result disagrees with observations in human kidneys and conceivably might be because of the inclusion of partial volumes of the adjacent renal pelvis in the image section.

### Qualitative Comparison With NIRS

The estimates of occlusion-induced changes in renal BVf and $SO_2$ obtained from MRI were benchmarked against quantitative parameters obtained for the renal cortex by means of NIRS. The relative changes (from baseline to VO) in cortical total hemoglobin concentration and $SO_2$ measured by NIRS were compared with the relative changes in cortical BVf and $SO_2$ derived from an ROI analysis on the MR parameter maps (Figure 9).

The MR data and NIRS data showed good agreement: cortical $SO_2$ decreased markedly during the short-term VO for both methods. The nearly 2-fold increase in cortical BVf measured with MRI during VO was mirrored by a similar increase in hemoglobin tissue concentration, as measured by NIRS. As for the injected USPIO, hemoglobin effectively serves as a naturally occurring label in the blood, and hence, its tissue concentration may be regarded as a surrogate for BVf, as long as the hematocrit remains unchanged.

## DISCUSSION

This work makes an important contribution to the literature on renal functional MRI by assessing changes in the renal BVf and in the renal $SO_2$ in response to VO. To achieve this goal, BVf measurements were implemented for rat kidneys at 9.4 T, including a dose-finding study for the intravascular contrast agent ferumoxytol. Multiparametric analysis was performed to estimate renal $SO_2$. Occlusion-induced changes in BVf and $SO_2$ derived from MRI were benchmarked against BVf and $SO_2$ references obtained from NIRS. Our main findings are that (1) a 4 mg of Fe/kg dose of ferumoxytol is suitable for BVf measurements at 9.4 T using baseline, VO and recovery; (2) the proposed approach provides high reproducibility for BVf and $SO_2$ assessment as demonstrated by the test–retest experiments; (3) relative changes in cortical BVf and cortical $SO_2$ derived from MRI were in accordance with relative changes in BVf and $SO_2$ deduced from NIRS; and (4) without the monitoring of BVf, MRI overestimates the $SO_2$ decrease during renal VO. The results of this work permitted a noninvasive detection of BVf increase upon VO and a removal of its effects on blood oxygenation-sensitized renal MR.

We found BVf to be higher in both outer and inner medulla than in the cortex, as shown by both $\Delta R_2$- and $\Delta R_2^*$-maps. Although these observations do not agree with recent results obtained by 3D microcomputed tomography (where cortical BVf was reported to be larger than medullary BVf) (56), they are in alignment with previous reports on $\Delta R_2$-based BVf estimates in rats and mice (38, 40), as well as with a series of earlier reports that measured renal BVf by means of (51) Cr-labelled red cells and $^{125}$I-γM-immunoglobulin: Rasmussen (55) reported medullary BVf in rats to be approximately twice the cortical BVf. There is no gold standard method, and the results provided by different techniques differ significantly. A hypointensity in $T_2^*$-weighted images had already suggested that BVf was higher in the medulla, but the $\Delta R_2^*$-maps depicted this even more clearly. The area with apparently very high BVf stretches from the papilla via the inner medulla to the central outer medulla. We hypothesize that these phenomena represent the influence of large Fe-rich vessels (57) located close to the image section, rather than the actual medullary tissue properties. The dissimilarity between $\Delta R_2$- and $\Delta R_2^*$-maps in revealing this area of unexpectedly high BVf further support our hypothesis: unlike $\Delta R_2^*$, $\Delta R_2$ is predominantly sensitive to small vessels and capillaries, because it relies on water diffusion within the near environment of the vessel walls, and the surface-to-volume ratio is highest for small vessel diameters. Hence, $\Delta R_2$ would be much less susceptible to the long-distance effects of a high amount of USPIO within extremely large blood vessels. Indeed, the locations of apparently high BVf in the papilla and inner medulla colocalize with the renal artery and vein, and the interlobar arteries and veins (56).

In the outer medulla, BVf displayed a rather high spatial heterogeneity and large spatial gradients along the longitudinal

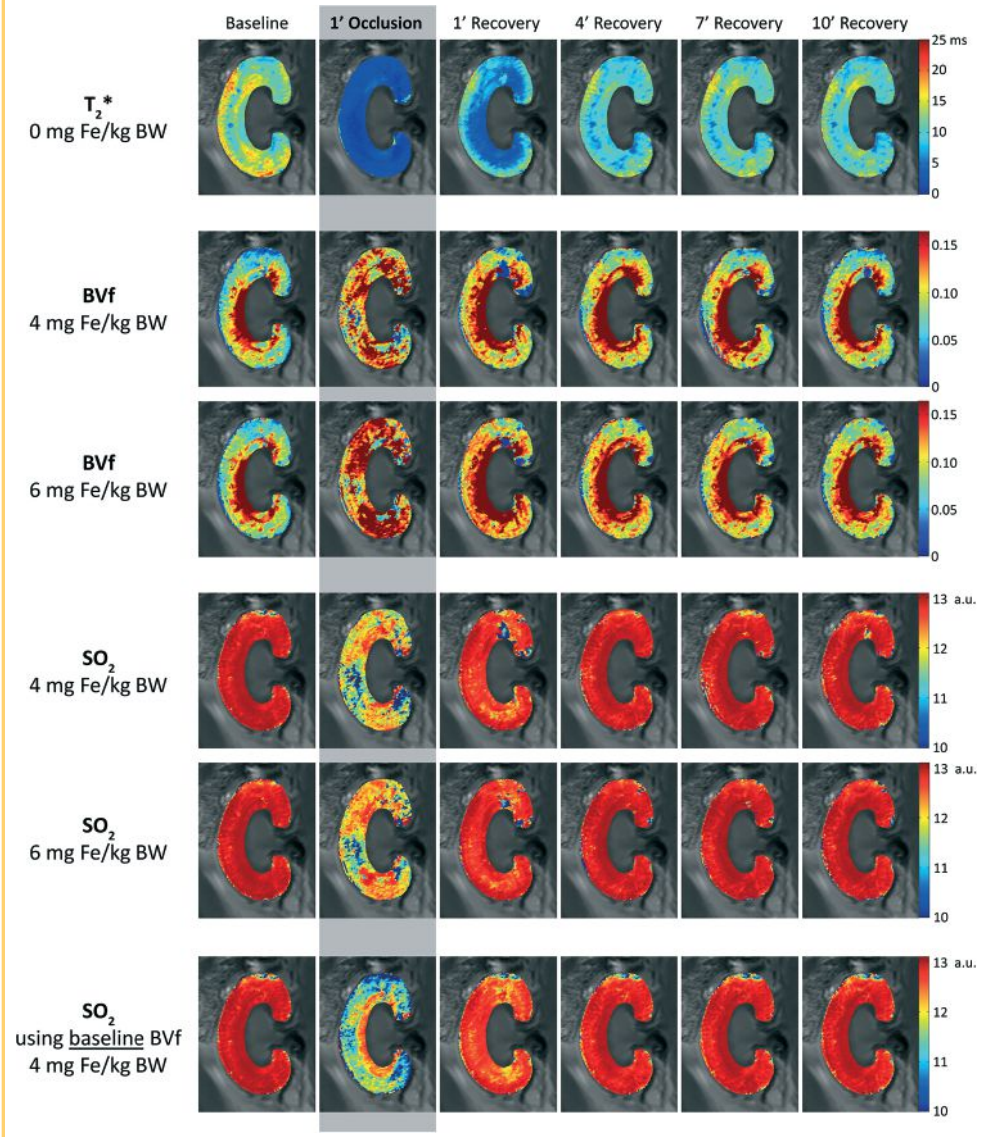


**Figure 8.** Maps of renal cortical and outer medullary $T_2^*$, together with estimated maps of BVf and oxygen saturation of hemoglobin ($SO_2$) at baseline, during VO and the recovery phase. The maps at baseline and after 10 min of recovery are almost indistinguishable, confirming that the effects of VO are reversible. Within-subject repeatability is demonstrated for renal BVf and $SO_2$ by comparing the maps derived from 2 different experimental phases, namely, *phase 3* (4 mg of Fe/kg USPIO) and *phase 4* (6 mg of Fe/kg USPIO). Test–retest reliability (repeatability) was high—the differences between both iterations are nearly negligible, even though more USPIO had been injected in between them. In addition, $SO_2$ maps were calculated assuming that renal BVf remains constant and identical to the baseline condition (bottom row): the missing compensation for BVf changes during VO results in $SO_2$ values being considerably lower than when BVf was monitored.

(rostral–caudal) axis. Here, large blood vessels (interlobar arteries and veins) surrounding the image section, as well as arcuate arteries and veins that run along the border between cortex and medulla (56), may play a role. Owing to the relatively large section thickness, the $T_2^*$-weighted images are considerably susceptible to magnetic field and frequency dispersions perpendicular to the image plane, created by large USPIO-loaded vessels. This hinders the assessment of the renal medulla. The choice of an axial section orientation or much thinner section thickness (if permitted by the SNR) could help resolve this issue. Despite these limitations, the variations in cortical BVf during renal VO were in good agreement with the results obtained from NIRS.

Our approach of parametric mapping of renal $T_2^*$ and $T_2$ made use of MGE and MSME techniques including respiratory triggering for respiratory motion compensation. The duration of each scan was 60–90 s, permitting a TR of ~3 min for interleaved $T_2^*$ and $T_2$ mapping. These protocols are available on clinical MR scanners, and hence it will be easily translatable to clinical use. The translation of our approach into the clinic is fueled by an increasing number of reports that eloquently speak of the off-label use of ferumoxytol for a broad spectrum of preclinical and diagnostic imaging applications (32, 43, 44, 58, 59). In the clinical setting, renal $T_2^*$ and $T_2$ mapping will most likely be used at time points that are at least hours, if not days or months, apart. In such a context, a 90-s delay between $T_2^*$ and $T_2$ scans appears to be short enough. Protocols affording breath-hold acquisitions could make respiratory triggering unnecessary, and parallel imaging capabilities are readily available on human MR scanners, both permitting acceleration of data acquisition.

In a laboratory setting, a higher temporal resolution might be needed to study some acute stimuli applied to animals. Fast physiological changes demand shorter scan durations and higher repetition rates. Imaging techniques that provide $T_2^*$- and $T_2$-weighted data (52, 60) provide an alternative to these preclinical applications. Fast spin-echo variants for $T_2$ and $T_2^*$ mapping permit choosing any desired $T_2^*$-weighting (including ultrashort times down to zero) and provide the extra benefit of being almost immune to image distortion (61, 62). Simultaneous dual-contrast 2-in-1 rapid acquisition with relaxation enhancement

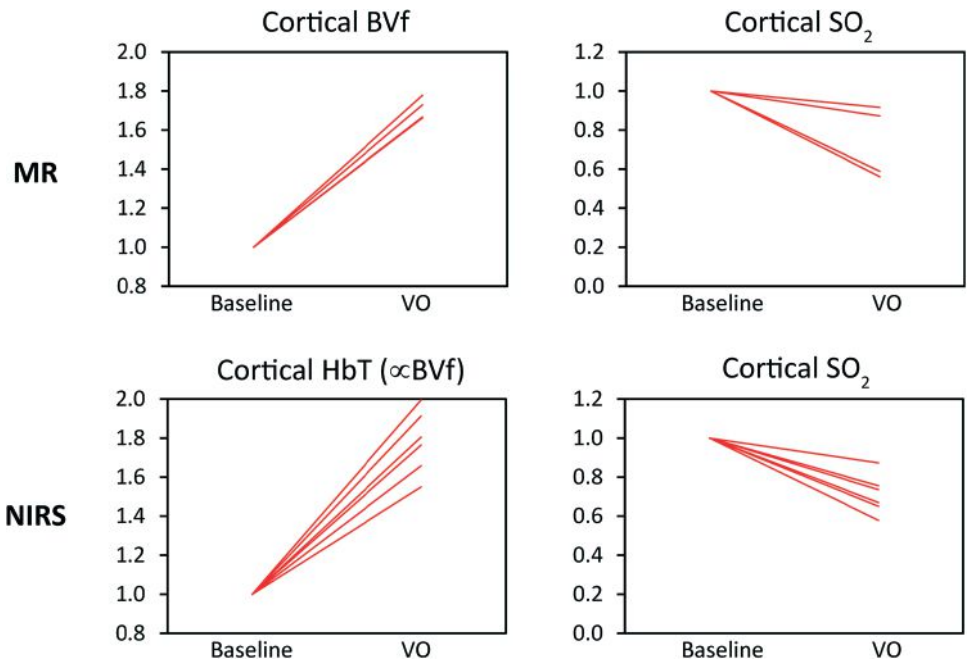


**Figure 9.** Relative changes in cortical BVf and $SO_2$ derived from the MR model analysis for the cortical ROIs (top panel; n = 4), referenced against related quantitative parameters obtained with near-infrared spectroscopy (NIRS; bottom panel; n = 6). HbT = total Hb concentration (per tissue volume). A large increase of BVf measured with MR during VO was mirrored by a similarly large increase in hemoglobin concentration measured by NIRS, which is considered a BVf surrogate. Cortical $SO_2$ derived from both methods decreased markedly during the short-term venous occlusion (VO).

presents a valuable alternative to sequential $T_2$- and $T_2^*$-weighted fast-spin echo acquisitions and promises to eliminate section-misregistration artifacts induced by bulk or physiological motions (63). Further enhancements of the SNR and spatial resolution could be gained by using cryogenically cooled RF coils in a preclinical setting (64, 65).

The multiparametric BOLD approach based on combining the monitoring of $T_2^*$ and $T_2$ with BVf has not previously been attempted for renal MR blood oximetry. This study demonstrates the feasibility of this approach in rats. A high reproducibility of $T_2^*$ and $T_2$ mapping and BVf measurements translated into $SO_2$ estimates with similarly high reproducibility.

The impact of the assumptions embedded in the model has previously been studied and it indicates that the model is sufficiently realistic (66) for the brain. The assumptions about the microvascular architecture should also hold for the kidney, except that the BVf used in the numerical study (4%) should be higher in renal tissue (literature values are contradictory but typically exceed 10%). However, because the model does not take into account the effects of renal tubuli, the presented study results may serve as only an approximate indicator for the usefulness of such a model-based approach and further investigation will be needed to advance the model for the kidney.

The current implementation of the model-based analysis has some methodological constraints that can be improved in future work. For the current study, intrarenal hematocrit was assumed to be 0.40, but, in fact, this value is known to vary throughout the kidney. Strategies to account for this may be necessary. To account for the susceptibility difference between blood with and without added ferumoxytol, a literature value of $\Delta\chi$ for a different USPIO of the same size and at the same magnetic field strength was used (50). It would be an added refinement to measure the $\Delta\chi$ for ferumoxytol and include it in the BVf calculations in the future. Because of our focus on fast, short-term changes in renal oxygenation, we assumed a constant magnetic field homogeneity, which might change modestly with respect to the kidney owing to respiratory motions and changes in renal size (renal tissue moves within $B_0$). $SO_2$ results were reported in arbitrary units because $B_0$ effects were not accounted for in this study. Our initial experiments (Figure 6) had shown that the effects of magnetic field inhomogeneity on renal $T_2^*$ were negligible after local shimming on the kidney, which we performed routinely. Generally, acquiring $B_0$-maps for each subject are recommended to permit a $B_0$ correction, if needed, and exclude a possible bias. Alternatively, acquiring high-resolution $T_2^*$ data makes a separate $B_0$ correction unnecessary owing to the reduced intravoxel dephasing (49, 67, 68), and it could represent an attractive way forward, presuming that the scan time penalty for increasing the spatial resolution is either of no relevance for the application or can be counteracted by strategies to accelerate acquisition. This can be accomplished, for example, by using combined acquisition techniques that integrate a minimum of 2 imaging strategies for $T_2^*$ and $T_2$ mapping (69).

Benchmarking BVf and $SO_2$ results against a quantitative reference is an obvious means of validating experimental results obtained from a novel MR technique. Currently, a perfect quantitative counterpart for MR-derived BVf and $SO_2$ is not available, as is the case for most MR techniques. Invasive tissue $pO_2$ probes can sample only very small regions, and they measure tissue $pO_2$ rather than blood oxygenation. NIRS allows measurements of the oxygen saturation of hemoglobin and tissue concentration of hemoglobin—a surrogate for BVf—but is currently limited to probing the cortex due to its low penetration depth. Comparisons between the occlusion-induced changes in cortical BVf and $SO_2$ obtained by MRI with the NIRS results for the cortex yield very good agreement, which should motivate the

further development of the MR approach proposed here into a comprehensive renal MR oximetry protocol.

In conclusion, this work established ferumoxytol-based steady-state MR measurements of renal BVfs for rats at a magnetic field strength of 9.4 T. Combining the BVf measurements with the monitoring of $T_2^*$ and $T_2$ allowed us to implement multiparametric quantitative BOLD MRI for the kidney as a promising approach *en route* renal blood oximetry. The findings are encouraging and should stimulate efforts to further improve this multiparametric technique, with the ultimate aim of translating it into clinical practice for the evaluation of AKIs and the development of chronic damage. Accomplishing this goal will require calibrations through simultaneous quantitative measurements with invasive physiological probes and NIRS in the same kidney. Once available to the clinicians, multiparametric renal MR oximetry will represent the first noninvasive method to reliably measure renal blood oxygenation. It could be combined with MR techniques for perfusion and diffusion (to probe tubular volume fraction) *en route* a comprehensive characterization of renal hemodynamics and tissue oxygenation, which may be an important biomarker for the early stages of a range of kidney diseases.

## ACKNOWLEDGMENTS

The authors wish to thank Thomas Christen (Stanford University, Stanford, USA) for very helpful discussions; Karen Arakelyan, Stefanie Münchberg, and Yvonne Balke (Max Delbrück Center for Molecular Medicine in the Helmholtz Association, Berlin, Germany) for the excellent technical support; Leili Riazy (Max Delbrück Center for Molecular Medicine in the Helmholtz Association, Berlin, Germany) for mathematical advice and Russell Hodge, and Jason Millward (Max Delbrück Center for Molecular Medicine in the Helmholtz Association, Berlin, Germany) for helping to prepare the manuscript. The present work was supported in part by the Deutsche Forschungsgemeinschaft (DFG, German Research Foundation; grant FOR1368, NI 532/9-2, SE 998/4-2) and the Bundesministerium für Bildung und Forschung (BMBF, German Ministry for Education and Research; grants VIP+ 03P00081 and VIP+ 03P00082).

Disclosures: No disclosures to report.

Conflict of Interest: The authors have no conflict of interest to declare.

## REFERENCES

1. Eckardt KU, Coresh J, Devuyst O, Johnson RJ, Kottgen A, Levey AS, Levin A. Evolving importance of kidney disease: from subspecialty to global health burden. Lancet. 2013;382(9887):158–169.
2. Lameire NH, Bagga A, Cruz D, De Maeseneer J, Endre Z, Kellum JA, Liu KD, Mehta RL, Pannu N, Van Biesen W, Vanholder R. Acute kidney injury: an increasing global concern. Lancet. 2013;382(9887):170–179.
3. Leung KC, Tonelli M, James MT. Chronic kidney disease following acute kidney injury-risk and outcomes. Nat Rev Nephrol. 2013;9(2):77–85.
4. Reuter S, Mrowka R. Acute kidney injury. Acta Physiol (Oxf). 2015;215(2):73–75.
5. Thakar CV, Christianson A, Freyberg R, Almenoff P, Render ML. Incidence and outcomes of acute kidney injury in intensive care units: a Veterans Administration study. Crit Care Med. 2009;37(9):2552–2558.
6. Thakar CV. Perioperative acute kidney injury. Adv Chronic Kidney Dis. 2013;20(1):67–75.
7. Ali T, Khan I, Simpson W, Prescott G, Townend J, Smith W, Macleod A. Incidence and outcomes in acute kidney injury: a comprehensive population-based study. J Am Soc Nephrol. 2007;18(4):1292–1298.
8. Sawhney S, Marks A, Fluck N, McLernon DJ, Prescott GJ, Black C. Acute kidney injury as an independent risk factor for unplanned 90-day hospital readmissions. BMC Nephrol. 2017;18(1):9.
9. Sawhney S, Marks A, Fluck N, Levin A, Prescott G, Black C. Intermediate and long-term outcomes of survivors of acute kidney injury episodes: a large population-based cohort study. Am J Kidney Dis. 2017;69(1):18–28.
10. Pickkers P, Ostermann M, Joannidis M, Zarbock A, Hoste E, Bellomo R, Prowle J, Darmon M, Bonventre JV, Forni L, Bagshaw SM, Schetz M. The intensive care medicine agenda on acute kidney injury. Intensive Care Med. 2017. [Epub ahead of print].
11. Schrezenmeier EV, Barasch J, Budde K, Westhoff T, Schmidt-Ott KM. Biomarkers in acute kidney injury – pathophysiological basis and clinical performance. Acta Physiol (Oxf). 2017;219(3):554–572.
12. Molitoris BA. Urinary Biomarkers: Alone Are They Enough? J Am Soc Nephrol. 2015;26(7):1485–1488.
13. Zarjou A, Sanders PW, Mehta RL, Agarwal A. Enabling innovative translational research in acute kidney injury. Clin Transl Sci. 2012;5(1):93–101.
14. Evans RG, O'Connor PM. Initiation and progression of chronic kidney disease: can we definitively test the chronic hypoxia hypothesis? Hypertension. 2013;62(5):827–828.
15. Persson PB. Renoprotection. Acta Physiol (Oxf). 2017;219(3):540–541.
16. Matejovic M, Ince C, Chawla LS, Blantz R, Molitoris BA, Rosner MH, Okusa MD, Kellum JA, Ronco C. Renal Hemodynamics in AKI: In Search of New Treatment Targets. J Am Soc Nephrol. 2016;27(1):49–58.
17. Khwaja A. KDIGO clinical practice guidelines for acute kidney injury. Nephron Clin Pract. 2012;120(4):c179–c184.
18. Grenier N, Merville P, Combe C. Radiologic imaging of the renal parenchyma structure and function. Nat Rev Nephrol. 2016;12(6):348–359.
19. Singh P, Ricksten SE, Bragadottir G, Redfors B, Nordquist L. Renal oxygenation and haemodynamics in acute kidney injury and chronic kidney disease. Clin Exp Pharmacol Physiol. 2013;40(2):138–147.
20. Evans RG, Goddard D, Eppel GA, O'Connor PM. Factors that render the kidney susceptible to tissue hypoxia in hypoxemia. Am J Physiol Regul Integr Comp Physiol. 2011;300(4):R931–R940.
21. Evans RG, Ince C, Joles JA, Smith DW, May CN, O'Connor PM, Gardiner BS. Haemodynamic influences on kidney oxygenation: clinical implications of integrative physiology. Clin Exp Pharmacol Physiol. 2013;40(2):106–122.
22. Chawla LS, Kimmel PL. Acute kidney injury and chronic kidney disease: an integrated clinical syndrome. Kidney Int. 2012;82(5):516–524.
23. Seeliger E, Sendeski M, Rihal CS, Persson PB. Contrast-induced kidney injury: mechanisms, risk factors, and prevention. Eur Heart J. 2012;33(16):2007–2015.
24. Legrand M, Mik EG, Johannes T, Payen D, Ince C. Renal hypoxia and dysoxia after reperfusion of the ischemic kidney. Mol Med. 2008;14(7-8):502–516.
25. Fahling M, Seeliger E, Patzak A, Persson PB. Understanding and preventing contrast-induced acute kidney injury. Nat Rev Nephrol. 2017;13(3):169–180.
26. Hansell P, Welch WJ, Blantz RC, Palm F. Determinants of kidney oxygen consumption and their relationship to tissue oxygen tension in diabetes and hypertension. Clin Exp Pharmacol Physiol. 2013;40(2):123–137.
27. Ogawa S, Lee TM, Kay AR, Tank DW. Brain magnetic resonance imaging with contrast dependent on blood oxygenation. Proc Natl Acad Sci U S A. 1990;87(24):9868–9872.
28. Neugarten J. Renal BOLD-MRI and assessment for renal hypoxia. Kidney Int. 2012;81(7):613–614.
29. Zhang JL, Morrell G, Rusinek H, Sigmund EE, Chandarana H, Lerman LO, Prasad PV, Niles D, Artz N, Fain S, Vivier PH, Cheung AK, Lee VS. New magnetic resonance imaging methods in nephrology. Kidney Int. 2014;85(4):768–778.
30. Niendorf T, Pohlmann A, Arakelyan K, Flemming B, Cantow K, Hentschel J, Grosenick D, Ladwig M, Reimann H, Klix S, Waiczies S, Seeliger E. How bold is blood oxygenation level-dependent (BOLD) magnetic resonance imaging of the kidney? Opportunities, challenges and future directions. Acta Physiol (Oxf). 2015;213(1):19–38.
31. Pohlmann A, Arakelyan K, Hentschel J, Cantow K, Flemming B, Ladwig M, Waiczies S, Seeliger E, Niendorf T. Detailing the relation between renal $T_2^*$ and renal tissue pO2 using an integrated approach of parametric magnetic resonance imaging and invasive physiological measurements. Invest Radiol. 2014;49(8):547–560.
32. Grosenick D, Cantow K, Arakelyan K, Wabnitz H, Flemming B, Skalweit A, Ladwig M, Macdonald R, Niendorf T, Seeliger E. Detailing renal hemodynamics and oxygenation in rats by a combined near-infrared spectroscopy and invasive probe approach. Biomed Opt Express. 2015;6(2):309–323.
33. Niendorf T, Flemming B, Evans RG, Seeliger E. What Do BOLD MR Imaging Changes in Donors' Remaining Kidneys Tell Us? Radiology. 2016;281(2):653–655.

34. Prasad PV. Functional MRI of the kidney: tools for translational studies of pathophysiology of renal disease. Am J Physiol Renal Physiol. 2006;290(5):F958–F974.
35. Bokacheva L, Rusinek H, Zhang JL, Lee VS. Assessment of renal function with dynamic contrast-enhanced MR imaging. Magn Reson Imaging Clin N Am. 2008; 16(4):597–611.
36. Aumann S, Schoenberg SO, Just A, Briley-Saebo K, Bjornerud A, Bock M, Brix G. Quantification of renal perfusion using an intravascular contrast agent (part 1): results in a canine model. Magn Reson Med. 2003;49(2):276–287.
37. Pedersen M, Laustsen C, Perot V, Basseau F, Moonen C, Grenier N. Renal hemodynamics and oxygenation in transient renal artery occluded rats evaluated with iron-oxide particles and oxygenation-sensitive imaging. Z Med Phys. 2010;20(2): 134–142.
38. Storey P, Ji L, Li LP, Prasad PV. Sensitivity of USPIO-enhanced R2 imaging to dynamic blood volume changes in the rat kidney. J Magn Reson Imaging. 2011; 33(5):1091–1099.
39. Wang YX. Current status of superparamagnetic iron oxide contrast agents for liver magnetic resonance imaging. World J Gastroenterol. 2015;21(47):13400–13402.
40. Wang F, Jiang RT, Tantawy MN, Borza DB, Takahashi K, Gore JC, Harris RC, Takahashi T, Quarles CC. Repeatability and sensitivity of high resolution blood volume mapping in mouse kidney disease. J Magn Reson Imaging. 2014;39(4): 866–871.
41. Tropres I, Lamalle L, Peoc'h M, Farion R, Usson Y, Decorps M, Remy C. In vivo assessment of tumoral angiogenesis. Magn Reson Med. 2004;51(3):533–541.
42. Pohlmann A, Karczewski P, Ku MC, Dieringer B, Waiczies H, Wisbrun N, Kox S, Palatnik I, Reimann HM, Eichhorn C, Waiczies S, Hempel P, Lemke B, Niendorf T, Bimmler M. Cerebral blood volume estimation by ferumoxytol-enhanced steady-state MRI at 9.4 T reveals microvascular impact of alpha1-adrenergic receptor antibodies. NMR Biomed. 2014;27(9):1085–1093.
43. Bashir MR, Bhatti L, Marin D, Nelson RC. Emerging applications for ferumoxytol as a contrast agent in MRI. J Magn Reson Imaging. 2015;41(4):884–898.
44. Hope MD, Hope TA, Zhu C, Faraji F, Haraldsson H, Ordovas KG, Saloner D. Vascular imaging with ferumoxytol as a contrast agent. AJR Am J Roentgenol. 2015;205(3):W366–W373.
45. Ning P, Zucker EJ, Wong P, Vasanawala SS. Hemodynamic safety and efficacy of ferumoxytol as an intravenous contrast agent in pediatric patients and young adults. Magn Reson Imaging. 2016;34(2):152–158.
46. Cantow K, Pohlmann A, Flemming B, Ferrara F, Waiczies S, Grosenick D, Niendorf T, Seeliger E. Acute effects of ferumoxytol on regulation of renal hemodynamics and oxygenation. Sci Rep. 2016;6:29965.
47. Budjan J, Neudecker S, Schock-Kusch D, Kraenzlin B, Schoenberg SO, Michaely HJ, Attenberger UI. Can Ferumoxytol be used as a contrast agent to differentiate between acute and chronic inflammatory kidney disease? Feasibility study in a rat model. Invest radiol. 2016;51(2):100–105.
48. Boxerman JL, Hamberg LM, Rosen BR, Weisskoff RM. MR contrast due to intravascular magnetic susceptibility perturbations. Magn Reson Med. 1995;34(4): 555–566.
49. Christen T, Lemasson B, Pannetier N, Farion R, Segebarth C, Remy C, Barbier EL. Evaluation of a quantitative blood oxygenation level-dependent (qBOLD) approach to map local blood oxygen saturation. NMR Biomed. 2011;24(4): 393–403.
50. Kim T, Hendrich KS, Masamoto K, Kim SG. Arterial versus total blood volume changes during neural activity-induced cerebral blood flow change: implication for BOLD fMRI. J Cereb Blood Flow Metab. 2007;27(6):1235–1247.
51. Pohlmann A, Hentschel J, Fechner M, Hoff U, Bubalo G, Arakelyan K, Cantow K, Seeliger E, Flemming B, Waiczies H, Waiczies S, Schunck WH, Dragun D, Niendorf T. High temporal resolution parametric MRI monitoring of the initial ischemia/reperfusion phase in experimental acute kidney injury. PloS One. 2013; 8(2):e57411.
52. He X, Yablonskiy DA. Quantitative BOLD: mapping of human cerebral deoxygenated blood volume and oxygen extraction fraction: default state. Magn Reson Med. 2007;57(1):115–126.
53. Yablonskiy DA, Haacke EM. Theory of NMR signal behavior in magnetically inhomogeneous tissues: the static dephasing regime. Magn Reson Med. 1994; 32(6):749–763.
54. Spees WM, Yablonskiy DA, Oswood MC, Ackerman JJ. Water proton MR properties of human blood at 1.5 Tesla: magnetic susceptibility, T(1), T(2), T*(2), and non-Lorentzian signal behavior. Magn Reson Med. 2001;45(4):533–542.
55. Rasmussen SN. Intrarenal red cell and plasma volumes in the non-diuretic rat. Determination by means of 51Cr labelled red cells and 125I-gamma-M-immunoglobulin. Pflugers Arch. 1973;342(1):61–72.
56. Garcia-Sanz A, Rodriguez-Barbero A, Bentley MD, Ritman EL, Romero JC. Three-dimensional microcomputed tomography of renal vasculature in rats. Hypertension. 1998;31(1 Pt 2):440–444.
57. Marxen M, Sled JG, Yu LX, Paget C, Henkelman RM. Comparing microsphere deposition and flow modeling in 3D vascular trees. Am J Physiol Heart Circ Physiol. 2006;291(5):H2136–H2141.
58. Fananapazir G, Bashir MR, Corwin MT, Lamba R, Vu CT, Troppmann C. Comparison of ferumoxytol-enhanced MRA with conventional angiography for assessment of severity of transplant renal artery stenosis. J Magn Reson Imaging. 2017; 45(3):779785.
59. Corwin MT, Fananapazir G, Chaudhari AJ. MR angiography of renal transplant vasculature with ferumoxytol: comparison of high-resolution steady-state and first-pass acquisitions. Acad Radiol. 2016;23(3):368–373.
60. Ma J, Wehrli FW. Method for image-based measurement of the reversible and irreversible contribution to the transverse-relaxation rate. J Magn Reson B. 1996; 111(1):61–69.
61. Heinrichs U, Utting JF, Frauenrath T, Hezel F, Krombach GA, Hodenius MA, Kozerke S, Niendorf T. Myocardial $T_2^*$ mapping free of distortion using susceptibility-weighted fast spin-echo imaging: a feasibility study at 1.5 T and 3.0 T. Magn Reson Med. 2009;62(3):822–828.
62. Niendorf T. On the application of susceptibility-weighted ultra-fast low-angle RARE experiments in functional MR imaging. Magn Reson Med. 1999;41(6): 1189–1198.
63. Fuchs K, Hezel F, Klix S, Mekle R, Wuerfel J, Niendorf T. Simultaneous dual contrast weighting using double echo rapid acquisition with relaxation enhancement (RARE) imaging. Magn Reson Med. 2014;72(6):1590–1598.
64. Wagenhaus B, Pohlmann A, Dieringer MA, Els A, Waiczies H, Waiczies S, Schulz-Menger J, Niendorf T. Functional and morphological cardiac magnetic resonance imaging of mice using a cryogenic quadrature radiofrequency coil. PloS One. 2012;7(8):e42383.
65. Niendorf T, Pohlmann A, Reimann HM, Waiczies H, Peper E, Huelnhagen T, Seeliger E, Schreiber A, Kettritz R, Strobel K, Ku MC, Waiczies S. Advancing cardiovascular, neurovascular, and renal magnetic resonance imaging in small rodents using cryogenic radiofrequency coil technology. Front Pharmacol. 2015; 6:255.
66. Christen T, Zaharchuk G, Pannetier N, Serduc R, Joudiou N, Vial JC, Remy C, Barbier EL. Quantitative MR estimates of blood oxygenation based on $T_2^*$: a numerical study of the impact of model assumptions. Magn Reson Med. 2012; 67(5):1458–1468.
67. Hezel F, Thalhammer C, Waiczies S, Schulz-Menger J, Niendorf T. High spatial resolution and temporally resolved $T_2^*$ mapping of normal human myocardium at 7.0 Tesla: an ultrahigh field magnetic resonance feasibility study. PloS One. 2012;7(12):e52324.
68. Huelnhagen T, Hezel F, Serradas Duarte T, Pohlmann A, Oezerdem C, Flemming B, Seeliger E, Prothmann M, Schulz-Menger J, Niendorf T. Myocardial effective transverse relaxation time $T_2^*$ correlates with left ventricular wall thickness: a 7.0 T MRI study. Magn Reson Med. 2017;77(6):2381–2389.
69. Jakob PM, Hillenbrand CM, Kenn W, Hahn D, Haase A. Abdominal imaging with a modular combination of spin and gradient echoes. Magn Reson Med. 2002;47(3):425–432.